

**Emergence of deep convection in the Arctic  
Ocean under a warming climate.**

**Camille Lique<sup>1</sup>, Helen L. Johnson<sup>2</sup>, Yves Plancherel<sup>2</sup>.**

<sup>1</sup> Laboratoire d'Océanographie Physique et Spatiale, UMR6523, CNRS-Ifremer-UBO-IRD, Brest, France,

<sup>2</sup> Department of Earth Sciences, University of Oxford, Oxford, UK,

e-mail: `Camille.Lique@ifremer.fr`

Received: date / Accepted: date

**Abstract.** The appearance of winter deep mixed layers in the Arctic Ocean under a warming climate is investigated with the HiGEM coupled global climate model. In response to a four times increase of atmospheric  $CO_2$  levels with respect to present day conditions, the Arctic Basin becomes seasonally ice-free. Its surface becomes consequently warmer and, on average, slightly fresher. Locally, changes in surface salinity can be far larger (up to 4 psu) than the basin-scale average, and of a different sign. The Canadian Basin undergoes a strong freshening, while the Eurasian Basin undergoes strong salinification. These changes are driven by the spin up of the surface circulation, likely resulting from the increased transfer of momentum to the ocean as sea ice cover is reduced. Changes in the surface salinity field also result in a change in stratification, which is strongly enhanced in the Canadian Basin and reduced in the Eurasian Basin. Reduction, or even suppression, of the stratification in the Eurasian Basin produces an environment that is favourable for, and promotes the appearance of, deep convection near the sea ice edge, leading to a significant deepening of winter mixed layers in this region (down to 1000m). As the Arctic Ocean is transitioning toward a summer ice-free regime, new dynamical ocean processes will appear in the region, with potentially important consequences for the Arctic Ocean itself and for climate, both locally and on larger scales.

## 1 Introduction

The mixed layer at the surface of the ocean connects the atmosphere with the deep ocean. It allows for the exchange of buoyancy and momentum, as well as gases including oxygen and carbon dioxide, between the atmosphere and the ocean interior. In a few locations, the mixed layer episodically reaches depths of hundreds of metres, symptomatic of the formation of dense water. In the North Atlantic, deep convection events have been observed in the Labrador, Irminger and Greenland Seas (Marshall and Schott, 1999; Pickart et al., 2003). These regions are all characterized by the seasonally intermittent presence of sea ice, and the deepest mixed layers are often observed near the sea ice edge, where large horizontal temperature and salinity gradients can be found at the ocean surface. Juxtaposition of ice-free and ice-covered areas accentuates the intensity of air-sea exchange over the ocean, resulting in buoyancy loss and water mass transformation (Griffies et al., 2009; Våge et al., 2009; Germe et al., 2011). In contrast, the mixed layer in the Arctic Ocean is much shallower (Peralta-Ferriz and Woodgate, 2015); the near-perennial presence of sea ice and the strong surface stratification insulate the ocean from intense air-sea exchange, limiting buoyancy loss and momentum input into the upper ocean.

As part of the fifth phase of the Climate Model Intercomparison Project (CMIP5; Taylor et al., 2012), the projected climate conditions in the North Atlantic and the Arctic have been examined in a series of coupled climate models forced with a range of increasing greenhouse gas emission scenarios. Although the CMIP5 models exhibit a large spread in their results, they largely agree on the direction of change for several key climate features. These include a decline in the Atlantic Meridional Overturning Circulation (AMOC) (Cheng et al., 2013), a large shoaling of the Mixed Layer Depths (MLDs) in the North Atlantic and in particular in the Labrador Sea (Heuzé et al.,

2015), indicating a decrease in the intensity of deep convection, and a decline in Arctic sea ice cover (Stroeve et al., 2012), along with a northward migration of the sea ice edge into the Arctic Ocean and the Barents Sea. Given that the location of deep convection sites is inherently tied to the location of the sea ice edge, one might expect that new regions of deep convection could appear at higher latitudes (Rainville et al., 2011). We expect that changes in deep convection location and MLD will alter water mass properties and ultimately the deep branch of the AMOC (Rahmstorf, 2002; Heuzé, 2017) and ocean heat transport (Exarchou et al., 2015).

Today, the deepest layers of the Canadian and Eurasian Basins are mostly filled with dense waters formed by brine rejection during sea ice formation on the continental shelves, or transformed in the Barents Sea, or advected from the Greenland Sea through Fram Strait. These dense water masses are eventually advected to the Nordic Seas through Fram Strait (Jones et al., 1995; Lique et al., 2010). As the sea ice edge migrates northward, the expectation is that the relative contribution of deep waters formed locally in the Arctic Basin by open ocean convection will increase relative to those waters formed on continental shelves or in the Barents Sea. In the deep Greenland Sea, observations suggest that the amount of dense water originating from the deep Arctic has recently increased compared to the dense water formed locally in the Greenland Sea during deep convection events (Langehaug and Falck, 2012; Somavilla et al., 2013). Moreover, Langehaug and Falck (2012) show that the export of dense water from the Arctic through Fram Strait has switched from being an intermittent to a permanent feature over the past decade, which indicates a change in the deep pressure gradient across Fram Strait.

The aim of the present study is to seek evidence for the emergence of deep convection areas in the high Arctic, as the sea ice edge moves northward. Our analysis is based on simulations from the



global coupled climate model HiGEM (Shaffrey et al., 2009) in which  $CO_2$  levels in the atmosphere drastically alter the radiative balance. The model and simulations used are briefly described in Section 2. In Section 3, we examine the present-day and future mixed layers as simulated in the model runs. Changes in MLD are then related to changes in sea ice conditions, atmospheric forcing and ocean dynamics in Section 4. Climatic consequences associated with changes in MLD are discussed in Section 5. A summary and conclusions are given in Section 6.

## 2 The numerical experiment

The simulations used in this study were performed with the High-Resolution Global Environmental Model (HiGEM), which is an ocean–sea ice–atmosphere coupled model based on the Hadley Centre Global Environmental Model version 1 (HadGEM1; Johns et al., 2006). A full description and basic evaluation of the HiGEM model can be found in Shaffrey et al. (2009). It uses a spherical latitude-longitude grid with an atmospheric horizontal resolution of  $0.83^\circ$  latitude  $\times$   $1.25^\circ$  longitude and 38 vertical levels, and a  $1/3^\circ \times 1/3^\circ$  resolution ocean with 40 unevenly-spaced levels in the vertical. For the ocean component, parameterizations include a scale-selective biharmonic scheme for the momentum dissipation, the isopycnal formulation of Griffies et al. (1998) with constant isopycnal diffusivity for the lateral mixing of tracers, and a biharmonic scheme to represent enhanced horizontal mixing of temperature and salinity in the upper 20 m. Eddies are permitted at mid and low latitudes and are parameterized at high latitudes by the Gent and McWilliams (1990) adiabatic mixing scheme with a latitudinally varying thickness diffusion coefficient, and the adiabatic biharmonic scheme of Roberts and Marshall (1998). The mixed layer scheme is based on the Richardson number parametrization, subject to minimum depth-dependent background diffusivity and viscosity, following Kraus and Turner (1967). The sea-ice model is an adaptation of the Community Ice Code (CICE; Hunke and Dukowicz, 1997), that uses an elastic-viscous-plastic rheology and

a five-category ice thickness distribution, but an independent zero-layer thermodynamics scheme (McLaren et al., 2006). The ocean and the atmosphere are initialized from rest using data from the World Ocean Atlas 2001 (Boyer et al., 2005) and the ECMWF analysis, respectively.

Two simulations are analyzed. The first is a 130 year control integration (labelled CTRL) in which greenhouse gases are kept constant at close to present-day concentrations (the concentrations of  $CO_2$ ,  $CH_4$ , and  $N_2O$  are 345 ppm, 1656 ppb, and 307 ppb, respectively). The second simulation (labelled  $4\times CO_2$ ) is initialized from the CTRL simulation at year 30 and then integrated for 100 years. For this integration, the atmospheric concentration of  $CO_2$  is increased by 2% per year for 70 years until levels reach 4 times that of the control run, and are then kept constant for a further 30 years. The rate of  $CO_2$  increase in this simulation is roughly twice as large as that in the least conservative scenario used for the IPCC AR5 (RCP 8.5), but the increase is not as sustained and plateaus at a value that is 30% lower. The idealized forcing allows for a clearer assessment of the response to radiative forcing than a simulation with more complicated scenarios of future radiative forcing. It is clear that the two simulations used in this study are much shorter than the time required to bring the ocean-atmosphere system into an equilibrated state with no memory of the somewhat arbitrary initial conditions (Covey et al., 2006). With this potential shortcoming in mind, we note that a strong adjustment takes place over the first 20–30 years of the *CTRL* simulation, and we thus choose to discard the first 30 years of the simulation from our analyses.

For the present study, we use 10 years of each simulation (years 120 to 129), in order to focus on the signal of interest here (i.e. the emergence of deep convection in the High Arctic). Monthly outputs over the 10 years are averaged month by month to create a climatological year for each simulation. In the following, we discuss particularly the averages for the months of March and

September, as these are representative of the periods when the two extrema of the seasonal cycles in MLD and sea ice extent occur. For all the variables presented in this paper, the significance of the difference between the two simulations is assessed by comparing the difference field with two standard deviations of the same variable, computed from 100 years of monthly or annual means in the *CTRL* run. To first order, this diagnostic allows us to distinguish between change driven by the radiative forcing and change that could potentially come from internal decadal variability of the ocean–atmosphere system.

### 3 Change in mixed layer depth

In this section, we examine the properties of the ocean surface and the mixed layer as simulated by the HiGEM model. The investigation of differences between the  $4\times CO_2$  and the *CTRL* simulations allows us to determine the ocean and sea ice responses to increasing levels of  $CO_2$  in the atmosphere.

Fig. 1 shows the mean MLD in March and September and the mean location of the sea ice edge over the last 10 years of the *CTRL* and  $4\times CO_2$  simulations, as well as the differences between the two runs. For each grid point, MLD is computed from monthly mean averages and the density is evaluated using the EOS80 formulation (Fofonoff, 1985), consistent with the equation of state used in HiGEM. MLD is then determined based on a density difference from the surface of  $\Delta\sigma = 0.03kg/m^3$ , following the criteria chosen in previous Arctic-focused studies (Toole et al., 2010; Jackson et al., 2012). Note that the results show little sensitivity to the choice of threshold, as long as this is expressed in term of density. Stratification in the Arctic is mostly determined by salinity, and thus a temperature criterion, as often used in other part of the globe, is not a suitable definition of MLD there.

For the *CTRL* simulation, a classical pattern stands out, with MLD in March reaching greater than 800m in typical deep convection areas (i.e. the Labrador, Irminger and Nordic Seas and the Rockall Basin), and MLD in September much shallower ( $\sim 50m$ ). As is often the case with CMIP-type climate models (Heuzé et al., 2013), HiGEM tends to produce most of its dense water masses through convection in the open ocean rather than through shelf processes and further cascading of dense water. The magnitude and general pattern of MLD are in agreement with climatology based on observations using the same density criterion (de Boyer Montégut et al., 2004) (not shown). The deepest winter MLDs are located close to the sea ice edge or to steep bathymetry (or both), while MLDs do not exceed  $\sim 50m$  under sea ice.

Compared to the *CTRL* run, winter MLD in the  $4\times CO_2$  run is generally much shallower. MLDs in the areas where deep convection occurs in the *CTRL* run reach 300 – 400m in the  $4\times CO_2$  run, i.e roughly half the MLD found in the *CTRL* run. The strong shoaling of winter MLDs in the Labrador Sea in the  $4\times CO_2$  HiGEM run has been previously linked with the decrease of the AMOC (Thomas et al., 2012) and the weaker intensity of the Subpolar Gyre (Lique et al., 2015). In the Greenland Sea, the convective patch is displaced southward along the sea ice edge. This shift occurs at the same time as a strong intensification of the gyre in the Greenland Sea in the  $4\times CO_2$  run compared to the *CTRL* run, which has been previously related to a change in wind stress curl (Lique et al., 2015). Whilst MLD decreases in most existing deep convection locations, the difference in MLD between the two runs for the representative month of March also reveals that new areas of convection appear North of Svalbard and in the high Arctic. In these regions, MLD deepens by up to 400m in the  $4\times CO_2$  run compared to the *CTRL* run on average over the last 10 years of the runs. In the Arctic, the ‘new’ locations with deep winter MLDs correspond to regions that are ice free year round in the  $4\times CO_2$  run as both summer and winter sea ice edges move northward. A

similar deepening of the winter MLD in the Nansen Basin under the IPCC RCP8.5 scenario was found in a different coupled model by Brodeau and Koenigk (2016), although these authors did not investigate the origin of this signal.

We examine the time series of maximum MLD detected in different parts of the North Atlantic and the Arctic in the two runs (Fig. 2), to get a sense of the episodic nature of the convective events that appear in this region in the  $4\times CO_2$  run. One should remember that the  $4\times CO_2$  run is relatively short, and that Year 100 corresponds to the time when the atmospheric concentration of  $CO_2$  starts to plateau at its maximum value. In the Eurasian Basin, winter MLDs in the  $4\times CO_2$  run first diverge significantly from the *CTRL* run in March of year 67, but the convective events only become recurrent and intense (with MLD greater than 500m) at the very end of the run, corresponding to the time when the sea ice cover has become seasonal and the winter sea ice extent has also greatly reduced (Fig. 2(a)). The maximum MLD detected in the Eurasian Basin varies between 360m and 960m during the ten years analyzed in this study (years 120 to 129). It is also possible that the emergence of deep convection in the Nansen Basin could be a transient signal that would vanish again in a longer simulation (Brodeau and Koenigk, 2016). The time series of MLD in the Greenland Sea reveals a sharp transition (around Year 55) toward shallower MLD in the  $4\times CO_2$  run, unlike in the Labrador and Irminger Seas where MLD gradually decreases as the level of  $CO_2$  in the atmosphere increases.

In summer, MLDs in the  $4\times CO_2$  run generally become shallower where they were deepest in the *CTRL* run (Fig. 1). However, a deepening of the MLDs by  $\sim 40m$  is visible in the Arctic, principally North of the Kara and Barents Seas and Bering Strait. By the end of the  $4\times CO_2$  run, the Arctic is almost completely ice-free in summer (Fig. 2(a)). The ocean surface is thus in direct contact with

the atmosphere and the momentum input to the ocean increases, resulting in intensified wind-driven mixing (e.g. Rainville and Woodgate, 2009). A closer look at the monthly MLD seasonal cycle (using an EOF decomposition; not shown) reveals that the timing of the seasonal cycle is similar in the two simulations, with the shallowest MLD in summer (June to September) and the deepest MLD in winter (February to April).

#### 4 Emergence of favourable conditions for deep convection in the Arctic

We next examine the atmospheric, oceanic and sea ice conditions in the two runs, in order to understand what circumstances lead to a deepening of Arctic MLD in the  $4\times CO_2$  run. Figs. 3, 4 and 5 show the March and September Sea Surface Temperature (SST), Sea Surface Salinity (SSS) and surface potential density ( $\sigma$ ), respectively, averaged over the last 10 years of the *CTRL* and  $4\times CO_2$  simulations, as well as the differences between the two runs. Fig. 6 shows the mean seasonal cycle of the same quantities averaged over the region north of  $65^\circ N$ .

The changes affecting the SST in the Arctic are closely linked to the presence or absence of sea ice. By the end of the  $4\times CO_2$  run, the Arctic sea ice cover has become seasonal (Fig. 6(d)), leading to a strong summer warming of the surface layer throughout the whole basin: SST rises by  $6-8^\circ C$  in September in the  $4\times CO_2$  run compared to the *CTRL* run (Fig. 3 and 6(a)). In turn, the strong summer warming results in a strong increase in the amplitude of the SST seasonal cycle (Fig. 6(a)), given that the SST remains at the freezing point in winter in the  $4\times CO_2$  run over much of the basin, owing to the presence of sea ice (Fig. 3).

Such an increase in the amplitude of the Arctic SST seasonal cycle under a warming climate has also been documented previously in a set of CMIP5 coupled climate models (Carton et al., 2015).

Interestingly, as seen in Holland and Bitz (2003), the growth in the amplitude of the SST seasonal cycle occurs in spite of a decrease in amplitude of the seasonal cycle in air surface temperature, implying accompanying changes in the seasonality of air-sea fluxes (Fig. 6(f)). Over large parts of the Arctic, sea-ice is still present in winter in the  $4\times CO_2$  run and so winter SST still approaches the freezing point throughout the run (Fig. 3). Because more heat has accumulated in summer though, this means that, locally and overall for the region, heat fluxes out of the ocean have to intensify to restore winter SST conditions. The intensification in the air-sea fluxes can be seen in Fig. 6(f), which shows greater heat fluxes into the ocean during the longer sea ice-free period in summer and greater fluxes out of the ocean in winter in the  $4\times CO_2$  run compared to the CTRL run. Part of these changes might be due to cloud feedbacks, which may not be properly captured in the model (Shaffrey et al., 2009). The annual mean heat flux out of the ocean, averaged over the Arctic Basin, increases by  $\sim 30\%$  in the  $4\times CO_2$  run. Graham and Vellinga (2013) argue that this strong change in surface heat flux is, however, likely compensated by an increase in the advective ocean heat transport from the North Atlantic, resulting in only moderate changes to the total Arctic Ocean heat storage.

Carton et al. (2015) also examine the change in the SSS seasonal cycle in CMIP5 models under different greenhouse gas emission scenarios. They find that, across the models examined, the amplitude of the Arctic basin-averaged SSS seasonal cycle tends to decrease, along with the annual-mean basin-averaged SSS. The decrease in annual-mean basin-averaged SSS is found to be larger for the model runs under IPCC scenarios with higher greenhouse gas emissions. These findings also hold for HiGEM. The basin-averaged annual mean SSS decreases by  $\sim 0.5$  psu in the  $4\times CO_2$  HiGEM run, and the amplitude of the basin-scale average SSS seasonal cycle also decreases under a warming climate, with a stronger decrease in winter and roughly no change in summer (Fig. 6(b)). Carton

et al. (2015) attribute the decrease of the amplitude of the basin-averaged SSS seasonal cycle to the decline of the sea ice cover. Indeed, the primary driver of the SSS seasonal cycle in the Arctic is the intensity of sea ice melting and formation processes (Ding et al., 2016), which is strongly reduced when the sea ice volume decreases, as a smaller volume of sea ice is formed and melted every year.

Importantly, the spatial pattern of the change in SSS (Fig. 4) reveals strong differences between the Canadian Basin (where a strong freshening is visible) and the Eurasian Basin (where the ocean surface is becoming saltier). This pattern of change in SSS also exhibits seasonality: the changes on the Eurasian side of the Arctic Basin are intensified in summer, while the freshening in the Canadian Basin is strongest in winter. This contrast between the two basins leads to compensation at the basin scale, which is why the basin-averaged and annual mean changes appear to be relatively small. On the Arctic shelves, the SSS changes between the *CTRL* and  $4\times CO_2$  runs are overall less intense, even reversing sign between winter and summer in some parts of the Chukchi Sea and the Canadian shelves.

The large scale pattern of SSS change seen in the interior of the basin is linked with a change of the ocean circulation (Fig. 7). The strong positive SSH anomaly in the Canadian Basin reveals that the anticyclonic Beaufort Gyre experiences a strong spin up. In the Beaufort Gyre, the SSH variations are a good proxy for the variations of freshwater content (Proshutinsky and Johnson, 1997), and thus the SSH increase indicates a convergence and accumulation of freshwater in the gyre, similar to that recently observed in the Arctic, albeit to a lesser extent (e.g. Giles et al., 2012). In contrast, salty water is accumulated in the topographically constrained cyclonic circulation in the Eurasian Basin. The SSH change pattern (Fig. 7) reveals a strong decrease of the SSH in the Eurasian Basin, indicative of a stronger cyclonic gyre in that basin. This suggests that, in the



model, Atlantic Water entering the Arctic through Fram Strait tends to penetrate further around the Eurasian basin in the  $4\times CO_2$  run, while the branch of Atlantic Water recirculating just north of Fram Strait (e.g. Bourke et al., 1988) is stronger in the *CTRL* run. Atlantic Water in the  $4\times CO_2$  run also tends to remain longer at the surface in the Arctic Basin and only subducts under the mixed layer or the halocline when it reaches the St. Anna Trough, located on the northern shelf of the Barents Sea, East of Franz Joseph Land. The increase in intensity of the two gyres within the Arctic Basin occurs whilst (a) the net volume exchange through the various Arctic gateways does not differ by more than 10%, and (b) there is no significant change in pattern or intensity of sea level pressure between the two runs (not shown). This suggest that the spin up of the gyre must be at least partly a response to intensification of the ocean surface stress resulting from reduction of the sea ice cover, although the impact of sea ice reduction on momentum transfer to the ocean surface is strongly model-dependent and even its sign is still a matter of debate (e.g. Martin et al., 2014; Tsamados et al., 2014; Martin et al., 2016).

The mean warming and freshening of the Arctic surface both contribute to the decrease of the surface density, by  $0.5\text{ kg/m}^3$  on average (Fig. 6(c)). The decrease in annual mean basin-averaged density is due to both surface warming in summer and freshening in winter (Fig. 6(a, b)). Examining the spatial pattern of the change in surface density (Fig. 5), we find a similar pattern to that of salinity (Fig. 4), with lighter water in the Canadian Basin and denser in the Eurasian Basin in the  $4\times CO_2$  run compared to the *CTRL* run. The anomalies are of similar amplitude ( $\sim 3\text{ kg/m}^3$ ) and tend to compensate at the basin scale.

All these surface property changes, notably surface density, also affect the ocean stratification (Fig. 8). We define stratification as the density difference between a depth of 500m and the ocean

283 surface, in order to capture the change over the depth range of the halocline everywhere in the  
 284 Arctic Basin; however, using a shallower level (200m as in Capotondi et al. (2012)) results in  
 285 similar patterns of stratification change (not shown). As expected, the change in stratification is  
 286 mostly driven by changes in surface density, apparent from the similar patterns seen in Figs 5 and  
 287 8. Indeed, sub-surface changes in density at 500m do not exceed  $0.3 \text{ kg/m}^3$ . In the  $4\times\text{CO}_2$  run,  
 288 stratification becomes very weak in the Eurasian Basin. This provides a preconditioning favourable  
 289 for deep mixing to occur as soon as the sea ice edge retreats enough to allow for intense and localized  
 290 cooling of the ocean surface. In contrast, the surface stratification in the Canadian Basin is strongly  
 291 enhanced, which will tend to suppress vertical mixing and favour the formation of sea ice in winter  
 292 (Davis et al., 2016).

## 293 **5 Potential impacts for the Arctic Basin and beyond**

294 Changes in MLD and stratification in the Arctic Basin under a warming climate are expected to  
 295 have multiple profound effects, on the ocean and climate as well as on other components of the  
 296 Earth system, both locally in the Arctic and on a global scale.

297 First, the changes highlighted in sections 3 and 4 will have a large impact on the primary  
 298 production in the Arctic Basin, and also affect biogeochemical cycles, including the carbon cycle.  
 299 Arrigo and van Dijken (2011) have shown that the net primary production in the Arctic Basin  
 300 increased by 20% between 1998 and 2009 in response to the reduction in sea ice extent and the  
 301 increase in duration of the open water season. Duarte et al. (2012) also suggested that these changes  
 302 have resulted in a shift of the Arctic planktonic community towards smaller species. As the sea ice  
 303 cover will continue to retreat further and for longer each year, allowing more input of momentum  
 304 and light to the ocean, net primary production will likely continue to increase in the future. The  
 305 change in stratification is also an important factor determining the amount of primary production:

stratification limits the nutrient supply from the deep layers and inhibits phytoplankton growth. Given that the changes in stratification (Fig. 8) simulated by the HiGEM model are of opposite sign in the Eurasian and Canadian Basins, future change in basin-wide net primary production will depend on regional conditions in these two basins. Dependency on regional scale changes likely explains some of the discrepancy (in sign and amplitude) amongst CMIP5 model forecasts of Arctic primary production under a warming climate (Vancoppenolle et al., 2013). Changes in the biology, together with those in MLD, will also impact the biological and physical carbon pumps in the Arctic (which currently accounts for roughly 10% of net global carbon uptake (Bates and Mathis, 2009; MacGilchrist et al., 2014)), although predicting the impacts of increasing  $CO_2$  once again requires an understanding of changes on a regional scale.

Second, the deepening of the mixed layer in some parts of the Arctic Basin will impact ventilation of the Arctic interior. This could consequently affect the export of dense water through Fram Strait into the Nordic Seas, and modify the downstream properties governing the overflows over the Greenland-Scotland Ridge. At the end of the  $4\times CO_2$  run, the bottom density in the deep Eurasian Basin has increased by  $0.25\text{--}0.5\text{ kg/m}^3$  compared to the *CTRL* run (Fig. 9). This density change results from an increase in salinity by  $0.5\text{--}1$  psu. In contrast, the density at the bottom of the Canadian Basin remains roughly similar to that in the *CTRL* run. The bottom waters on the shallow Arctic shelves evolve differently from the deep waters in the basins. In HiGEM, most water masses found at the bottom on the shallow Arctic shelves become lighter, due to both a freshening and a warming. This is in agreement with results from Heuzé et al. (2015), who find a consistent change over the Arctic shelves when looking at the CMIP5 models under the RCP8.5 emissions scenario. They estimate a multi-model mean decrease in bottom density of  $0.62\text{ kg/m}^3$  averaged over the shelves shallower than 1000m north of  $60^\circ\text{N}$ . In HiGEM, the Kara Sea exhibits a mean trend that is very different to that on other Arctic shelves. Water masses at the bottom of the

Kara Sea become denser and saltier (Fig. 9). This salinification is linked with the thick ( $\sim 2m$ ) sea ice that persists in winter in the region, suggesting strong brine rejection during sea ice formation. Denser waters found at the bottom of the Eurasian Basin are likely a consequence of the deepening of the MLD described in Section 3, which occurs near the continental slope in the Eurasian Basin; dense waters formed by convection over the slope in that location will cascade to the bottom of the basin. Another process that could explain this bottom density increase is export of dense waters formed in the Kara Sea and in the St. Anna Trough. It is, however, very likely that, in the  $4\times CO_2$  run, the model overestimates the formation of dense water through open ocean convection and underestimates (or does not properly represent) the component formed through shelf-processes; this is a common bias of most coupled climate models (e.g., Heuzé et al., 2013).

The increase in bottom density remains confined to the Eurasian Basin in the HiGEM 130-year long  $4\times CO_2$  run. A section of density across Fram Strait, which is the only connection between the deep Arctic and the deep Nordic Seas, does not reveal any significant change between the two runs below 1000m (Fig. 10). In contrast, the upper layer becomes less dense, due to a freshening of the export to the North Atlantic on the western side of the strait and a warming of the Atlantic Water flowing into the Arctic on the eastern side of the strait. Note that the volume exported to the North Atlantic through the deeper part of Fram Strait is also roughly equal in the *CTRL* and  $4\times CO_2$  runs.

Based on observations of the deep Greenland Sea, Langehaug and Falck (2012) and Somavilla et al. (2013) have both suggested that the relative proportion of Arctic-origin dense water has increased compared to the dense water mass formed locally during convective events in the Greenland Sea. The Arctic-origin dense water they observe has formed on the Arctic shelves and subsequently filled the deep Arctic Basin. In the future, denser water formed in the Eurasian Basin and further

exported to the Greenland Sea could in principle modify the direct contribution of the Arctic Basin to the dense overflows in the Nordic Seas and thus to the deeper branch of the AMOC. We do not find evidence that deep hydrographic changes in the Arctic influence overflow properties in our short HiGEM experiment by the end of the  $4\times CO_2$  run, but we cannot rule out that such an effect could arise in the longer term.

## 6 Summary and conclusions

The depth of the mixed layer and its variations are important controls on a wide range of ocean processes, including upper ocean productivity, air-sea exchange processes and ventilation of the ocean interior. Examining the changes in MLD projected by CMIP5 models has thus been the focus of several recent studies that have pointed out a general tendency for shallowing in regions where deep mixed layers are presently observed in the North Atlantic (e.g., Heuzé et al., 2015) and the Southern Ocean (e.g., Sallée et al., 2013). However, these studies do not investigate the potential for emergence or migration of deep convection hotspots. Here we have used simulations from the high-resolution climate model HiGEM to show that new regions of deep convection may appear in the Arctic Basin under a warming climate.

In response to a strong increase in atmospheric  $CO_2$  concentrations, the Arctic Basin becomes seasonally ice-free, and the Arctic ocean surface becomes consequently much warmer and slightly fresher on average. Although this is in agreement with previous CMIP5 assessments (e.g., Carton et al., 2015), we argue that limiting the examination to average basin-scale changes hides more extreme and important local changes. While surface warming is spatially quite homogeneous across the whole Arctic Basin, changes in salinity are much more spatially variable: a strong freshening is observed in the Canadian Basin but a strong salinification occurs in the Eurasian Basin, due to

the intensification of the surface circulation in both basins, associated with sea ice retreat. These local changes in sea surface salinity are ultimately responsible for changes in surface density and stratification that do not reflect the average conditions of the basin: stratification is strongly enhanced in the Canadian Basin but strongly reduced in the Eurasian Basin. The drastic decrease in stratification in the Eurasian Basin results in conditions that promote the appearance of deep convection in that basin: the northward migration of the winter sea ice edge results in localized Eurasian air-sea buoyancy fluxes that induce severe local deepening of the mixed layers (down to 500m) in that region, able to ventilate the deep Arctic.

A northward retreat of the position of the sea ice edge in winter is a necessary first step for deep convection to occur in the Arctic Basin. Although most of the CMIP5 models and HiGEM predict that the transition toward a summer ice-free Arctic will only occur during the second half of the century (Stroeve et al., 2012; Wang and Overland, 2012), it has also been suggested that these projections of future sea ice conditions are likely too conservative, even under the most pessimistic emission scenario (Mahlstein and Knutti, 2012; Stroeve and Notz, 2015). This is due to the mis-representation of important feedbacks between the different components of the Arctic system (e.g., Lique et al., 2016) that results in an underestimation of the so-called 'Arctic amplification of climate change' (Serreze and Barry, 2011; Pithan and Mauritsen, 2014).

Unfortunately, the influence of new regions of deep mixed layers on the deep Arctic, and their subsequent effects on the Greenland Sea and possibly the Atlantic Meridional Overturning Circulation downstream, cannot be established with the current  $4\times CO_2$  model run. Owing to the high-resolution and computational requirements of HiGEM, and the fact that the largest changes were only observed at the end of the run, the available simulation is currently too short to inves-

401 tigate the consequences for the deep water with any confidence. The duration of the simulation is  
402 also too short to rule out the hypothesis that emergence of deep convection in the Eurasian Basin  
403 is a transient signal that would vanish as the surface temperature continues to increase (enhancing  
404 the surface stratification) associated with further sea ice retreat (Brodeau and Koenigk, 2016). Our  
405 results nonetheless indicate that ventilation of the Arctic by local deep mixing events is possible  
406 in a high  $CO_2$  future (and possibly sooner than forecast by the CMIP5 and HiGEM models, if  
407 the sea ice were to retreat sooner than predicted), and we expect that these changes would have  
408 important downstream ramifications for deep water formation processes and deep water properties  
409 in the North Atlantic. Probing the emergence of deep convection in the Arctic Basin in a variety  
410 of climate models at a variety of resolution forced with different emission scenario is needed to test  
411 the robustness of our findings based on the HiGEM model.

*Acknowledgements.* HLJ is grateful for funding from the Natural Environment Research Council (NERC) UK Overturning in the Subpolar North Atlantic Program (UK-OSNAP, NE/K010948/1). YP acknowledges support from NERC IRF NE/M017826/1. The coupled climate model was developed from the Met Office Hadley Centre Model by the UK High-Resolution Modelling (HiGEM) Project and the UK Japan Climate Collaboration (UJCC). HiGEM is supported by a NERC High Resolution Climate Modelling Grant (R8/H12/123). UJCC was supported by the Foreign and Commonwealth Office Global Opportunities Fund, and jointly funded by NERC and the DECC/Defra Met Office Hadley Centre Climate Programme (GA01101). The model integrations were performed using the Japanese Earth Simulator supercomputer, supported by JAMSTEC. The work of Pier Luigi Vidale and Malcolm Roberts in leading the effort in Japan is particularly valued. We are also grateful to Prof David Stevens for making the model data available. We thank two anonymous reviewers for their constructive comments on the paper.



## References

- Arrigo, K. R., van Dijken, G. L., 2011. Secular trends in Arctic Ocean net primary production. *Journal of Geophysical Research (Oceans)* 116.
- Bates, N. R., Mathis, J. T., 2009. The Arctic Ocean marine carbon cycle: evaluation of air-sea CO<sub>2</sub> exchanges, ocean acidification impacts and potential feedbacks. *Biogeosciences* 6, 2433–2459.
- Bourke, R. H., Weigel, A. M., Paquette, R. G., 1988. The westward turning branch of the West Spitsbergen Current. *Journal of Geophysical Research* 931, 14065–14077.
- Boyer, T., Levitus, S., Garcia, H., Locarnini, R. A., Stephens, C., Antonov, J., 2005. Objective analyses of annual, seasonal, and monthly temperature and salinity for the World Ocean on a 0.25° grid. *International Journal of Climatology* 25, 931–945.
- Brodeau, L., Koenigk, T., 2016. Extinction of the northern oceanic deep convection in an ensemble of climate model simulations of the 20th and 21st centuries. *Climate Dynamics* 46, 2863–2882.
- Capotondi, A., Alexander, M. A., Bond, N. A., Curchitser, E. N., Scott, J. D., 2012. Enhanced upper ocean stratification with climate change in the CMIP3 models. *Journal of Geophysical Research (Oceans)* 117.
- Carton, J. A., Ding, Y., Arrigo, K. R., Sep. 2015. The seasonal cycle of the Arctic Ocean under climate change. *Geophysical Research Letters* 42, 7681–7686.
- Cheng, W., Chiang, J. C., Zhang, D., 2013. Atlantic meridional overturning circulation (amoc) in cmip5 models: Rcp and historical simulations. *Journal of Climate* 26 (18), 7187–7197.
- Covey, C., Gleckler, P. J., Phillips, T. J., Bader, D. C., 2006. Secular trends and climate drift in coupled ocean-atmosphere general circulation models. *Journal of Geophysical Research (Atmospheres)* 111, D03107.
- Davis, P. E. D., Lique, C., Johnson, H. L., Guthrie, J. D., 2016. Competing Effects of Elevated Vertical Mixing and Increased Freshwater Input on the Stratification and Sea Ice Cover in a Changing Arctic Ocean. *Journal of Physical Oceanography* 46, 1531–1553.

- de Boyer Montégut, C., Madec, G., Fischer, A. S., Lazar, A., Iudicone, D., 2004. Mixed layer depth over the global ocean: An examination of profile data and a profile-based climatology. *Journal of Geophysical Research (Oceans)* 109 (C18), C12003.
- Ding, Y., Carton, J. A., Chepurin, G. A., Steele, M., Hakkinen, S., 2016. Seasonal heat and freshwater cycles in the Arctic Ocean in CMIP5 coupled models. *Journal of Geophysical Research (Oceans)* 121, 2043–2057.
- Duarte, C. M., Agustí, S., Wassmann, P., Arrieta, J. M., Alcaraz, M., Coello, A., Marbà, N., Hendriks, I. E., Holding, J., García-Zarandona, I., et al., 2012. Tipping elements in the arctic marine ecosystem. *Ambio* 41 (1), 44–55.
- Exarchou, E., Kuhlbrodt, T., Gregory, J. M., Smith, R. S., 2015. Ocean Heat Uptake Processes: A Model Intercomparison. *Journal of Climate* 28, 887–908.
- Fofonoff, N. P., 1985. Physical properties of seawater: A new salinity scale and equation of state for seawater. *Journal of Geophysical Research* 90, 3332–3342.
- Gent, P. R., McWilliams, J. C., 1990. Isopycnal Mixing in Ocean Circulation Models. *Journal of Physical Oceanography* 20, 150–160.
- Germe, A., Houssais, M.-N., Herbaut, C., Cassou, C., 2011. Greenland Sea sea ice variability over 1979-2007 and its link to the surface atmosphere. *Journal of Geophysical Research (Oceans)* 116 (C15).
- Giles, K. A., Laxon, S. W., Ridout, A. L., Wingham, D. J., Bacon, S., 2012. Western Arctic Ocean freshwater storage increased by wind-driven spin-up of the Beaufort Gyre. *Nature Geoscience* 5, 194–197.
- Graham, T., Vellinga, M., 2013. Heat budget of the upper Arctic Ocean under a warming climate. *Climate Dynamics* 40, 143–153.
- Griffies, S. M., Biastoch, A., Böning, C., Bryan, F., Danabasoglu, G., Chassignet, E. P., England, M. H., Gerdes, R., Haak, H., Hallberg, R. W., Hazeleger, W., Jungclaus, J., Large, W. G., Madec, G., Pirani, A., Samuels, B. L., Scheinert, M., Gupta, A. S., Severijns, C. A., Simmons, H. L., Treguier, A. M., Winton, M., Yeager, S., Yin, J., 2009. Coordinated Ocean-ice Reference Experiments (COREs). *Ocean*

- 474 Modelling 26, 1–46.
- 475 Griffies, S. M., Gnanadesikan, A., Pacanowski, R. C., Larichev, V. D., Dukowicz, J. K., Smith, R. D., 1998.
- 476 Isonneutral Diffusion in a z-Coordinate Ocean Model. *Journal of Physical Oceanography* 28, 805–830.
- 477 Heuzé, C., 2017. North atlantic deep water formation and amoc in cmip5 models. *Ocean Science Discussions*
- 478 2017, 1–22.
- 479 Heuzé, C., Heywood, K. J., Stevens, D. P., Ridley, J. K., 2013. Southern Ocean bottom water characteristics
- 480 in CMIP5 models. *Geophysical Research Letters* 40, 1409–1414.
- 481 Heuzé, C., Heywood, K. J., Stevens, D. P., Ridley, J. K., 2015. Changes in global ocean bottom properties
- 482 and volume transports in cmip5 models under climate change scenarios. *Journal of Climate* .
- 483 Holland, M. M., Bitz, C. M., 2003. Polar amplification of climate change in coupled models. *Journal of*
- 484 *Climate* 21, 221–232.
- 485 Hunke, E. C., Dukowicz, J. K., 1997. An Elastic Viscous Plastic Model for Sea Ice Dynamics. *Journal of*
- 486 *Physical Oceanography* 27, 1849.
- 487 Jackson, J. M., Williams, W. J., Carmack, E. C., 2012. Winter sea-ice melt in the Canada Basin, Arctic
- 488 Ocean. *Geophysical Research Letter* 39, 3603.
- 489 Johns, T. C., Durman, C. F., Banks, H. T., Roberts, M. J., McLaren, A. J., Ridley, J. K., Senior, C. A.,
- 490 Williams, K. D., Jones, A., Rickard, G. J., Cusack, S., Ingram, W. J., Crucifix, M., Sexton, D. M. H.,
- 491 Joshi, M. M., Dong, B.-W., Spencer, H., Hill, R. S. R., Gregory, J. M., Keen, A. B., Pardaens, A. K.,
- 492 Lowe, J. A., Bodas-Salcedo, A., Stark, S., Searl, Y., 2006. The New Hadley Centre Climate Model
- 493 (HadGEM1): Evaluation of Coupled Simulations. *Journal of Climate* 19, 1327.
- 494 Jones, E. P., Rudels, B., Anderson, L. G., 1995. Deep waters of the Arctic Ocean: origins and circulation.
- 495 *Deep Sea Research I* 42, 737–760.
- 496 Kraus, E. B., Turner, J. S., 1967. A one-dimensional model of the seasonal thermocline ii. the general
- 497 theory and its consequences. *Tellus* 19 (1), 98–106.

- 498 Langehaug, H. R., Falck, E., 2012. Changes in the properties and distribution of the intermediate and deep  
499 waters in the Fram Strait. *Progress in Oceanography* 96, 57–76.
- 500 Lique, C., Holland, M. M., Dibike, Y. B., Lawrence, D. M., Screen, J. A., 2016. Modeling the Arctic  
501 freshwater system and its integration in the global system: Lessons learned and future challenges. *Journal*  
502 *of Geophysical Research (Biogeosciences)* 121, 540–566.
- 503 Lique, C., Johnson, H. L., Plancherel, Y., Flanders, R., 2015. Ocean change around Greenland under a  
504 warming climate. *Climate Dynamics* 45, 1235–1252.
- 505 Lique, C., Treguier, A. M., Blanke, B., Grima, N., 2010. On the origins of water masses exported along  
506 both sides of Greenland: A Lagrangian Model Analysis. *Journal of Geophysical Research* 115(C05019),  
507 5019.
- 508 MacGilchrist, G. A., Naveira Garabato, A. C., Tsubouchi, T., Bacon, S., Torres-Valdés, S., Azetsu-Scott,  
509 K., 2014. The Arctic Ocean carbon sink. *Deep Sea Research Part I: Oceanographic Research* 86, 39–55.
- 510 Mahlstein, I., Knutti, R., 2012. September Arctic sea ice predicted to disappear near 2°C global warming  
511 above present. *Journal of Geophysical Research (Atmospheres)* 117, D06104.
- 512 Marshall, J., Schott, F., 1999. Open-ocean convection: Observations, theory, and models. *Reviews of Geo-*  
513 *physics* 37 (1), 1–64.
- 514 Martin, T., Steele, M., Zhang, J., 2014. Seasonality and long-term trend of Arctic Ocean surface stress in  
515 a model. *Journal of Geophysical Research (Oceans)* 119, 1723–1738.
- 516 Martin, T., Tsamados, M., Schroeder, D., Feltham, D. L., 2016. The impact of variable sea ice roughness  
517 on changes in Arctic Ocean surface stress: A model study. *Journal of Geophysical Research (Oceans)*  
518 121, 1931–1952.
- 519 McLaren, A. J., Banks, H. T., Durman, C. F., Gregory, J. M., Johns, T. C., Keen, A. B., Ridley, J. K.,  
520 Roberts, M. J., Lipscomb, W. H., Connolley, W. M., Laxon, S. W., 2006. Evaluation of the sea ice simu-  
521 lation in a new coupled atmosphere-ocean climate model (HadGEM1). *Journal of Geophysical Research*  
522 *(Oceans)* 111 (C10), C12014.

- 523 Peralta-Ferriz, C., Woodgate, R. A., 2015. Seasonal and interannual variability of pan-arctic surface mixed  
524 layer properties from 1979 to 2012 from hydrographic data, and the dominance of stratification for  
525 multiyear mixed layer depth shoaling. *Progress in Oceanography* .
- 526 Pickart, R. S., Spall, M. A., Ribergaard, M. H., Moore, G., Milliff, R. F., 2003. Deep convection in the  
527 Irminger sea forced by the Greenland tip jet. *Nature* 424 (6945), 152–156.
- 528 Pithan, F., Mauritsen, T., 2014. Arctic amplification dominated by temperature feedbacks in contemporary  
529 climate models. *Nature Geoscience* 7, 181–184.
- 530 Proshutinsky, A. Y., Johnson, M. A., 1997. Two circulation regimes of the wind-driven Arctic Ocean.  
531 *Journal of Geophysical Research* 102, 12,493–12,514.
- 532 Rahmstorf, S., 2002. Ocean circulation and climate during the past 120,000 years. *Nature* 419, 207–214.
- 533 Rainville, L., Lee, C. M., Woodgate, R. A., 2011. Impact of wind-driven mixing in the Arctic ocean.  
534 *Oceanography-Oceanography Society* 24 (3), 136.
- 535 Rainville, L., Woodgate, R. A., 2009. Observations of internal wave generation in the seasonally ice-free  
536 Arctic. *Geophysical Research Letters* 36, L23604.
- 537 Roberts, M., Marshall, D., 1998. Do we require adiabatic dissipation schemes in eddy-resolving ocean  
538 models ? *Journal of Physical Oceanography* 28, 2050–2063.
- 539 Sallée, J.-B., Shuckburgh, E., Bruneau, N., Meijers, A. J. S., Bracegirdle, T. J., Wang, Z., 2013. Assessment  
540 of Southern Ocean mixed-layer depths in CMIP5 models: Historical bias and forcing response. *Journal*  
541 *of Geophysical Research (Oceans)* 118, 1845–1862.
- 542 Serreze, M. C., Barry, R. G., 2011. Processes and impacts of arctic amplification: A research synthesis.  
543 *Global and Planetary Change* 77 (1), 85–96.
- 544 Shaffrey, L. C., Stevens, I., Norton, W. A., Roberts, M. J., Vidale, P. L., Harle, J. D., Jrrar, A., Stevens,  
545 D. P., Woodage, M. J., Demory, M. E., Donners, J., Clark, D. B., Clayton, A., Cole, J. W., Wilson,  
546 S. S., Connolley, W. M., Davies, T. M., Iwi, A. M., Johns, T. C., King, J. C., New, A. L., Slingo, J. M.,  
547 Slingo, A., Steenman-Clark, L., Martin, G. M., 2009. U.K. HiGEM: The New U.K. High-Resolution

- Global Environment Model – Model Description and Basic Evaluation. *Journal of Climate* 22, 1861.
- Somavilla, R., Schauer, U., Budéus, G., 2013. Increasing amount of arctic ocean deep waters in the greenland sea. *Geophysical Research Letters* 40 (16), 4361–4366.
- Stroeve, J., Notz, D., 2015. Insights on past and future sea-ice evolution from combining observations and models. *Global and Planetary Change* 135, 119–132.
- Stroeve, J. C., Kattsov, V., Barrett, A., Serreze, M., Pavlova, T., Holland, M., Meier, W. N., 2012. Trends in Arctic sea ice extent from CMIP5, CMIP3 and observations. *Geophysical Research Letter* 39, 16502.
- Taylor, K. E., Stouffer, R. J., Meehl, G. A., 2012. An Overview of CMIP5 and the Experiment Design. *Bulletin of the American Meteorological Society* 93, 485–498.
- Thomas, M. D., de Boer, A. M., Stevens, D. P., Johnson, H. L., Aug. 2012. Upper ocean manifestations of a reducing meridional overturning circulation. *Geophysical Research Letter* 39, 16609.
- Toole, J. M., Timmermans, M.-L., Perovich, D. K., Krishfield, R. A., Proshutinsky, A., Richter-Menge, J. A., 2010. Influences of the ocean surface mixed layer and thermohaline stratification on Arctic Sea ice in the central Canada Basin. *Journal of Geophysical Research* 115 (C14), 10018.
- Tsamados, M., Feltham, D. L., Schroeder, D., Flocco, D., Farrell, S. L., Kurtz, N., Laxon, S. W., Bacon, S., 2014. Impact of Variable Atmospheric and Oceanic Form Drag on Simulations of Arctic Sea Ice\*. *Journal of Physical Oceanography* 44, 1329–1353.
- Våge, K., Pickart, R. S., Thierry, V., Reverdin, G., Lee, C. M., Petrie, B., Agnew, T. A., Wong, A., Ribergaard, M. H., 2009. Surprising return of deep convection to the subpolar North Atlantic Ocean in winter 2007–2008. *Nature Geoscience* 2.
- Vancoppenolle, M., Bopp, L., Madec, G., Dunne, J., Ilyina, T., Halloran, P. R., Steiner, N., 2013. Future arctic ocean primary productivity from cmip5 simulations: Uncertain outcome, but consistent mechanisms. *Global Biogeochemical Cycles* 27 (3), 605–619.
- Wang, M., Overland, J. E., 2012. A sea ice free summer Arctic within 30 years: An update from CMIP5 models. *Geophysical Research Letters* 39, L18501.

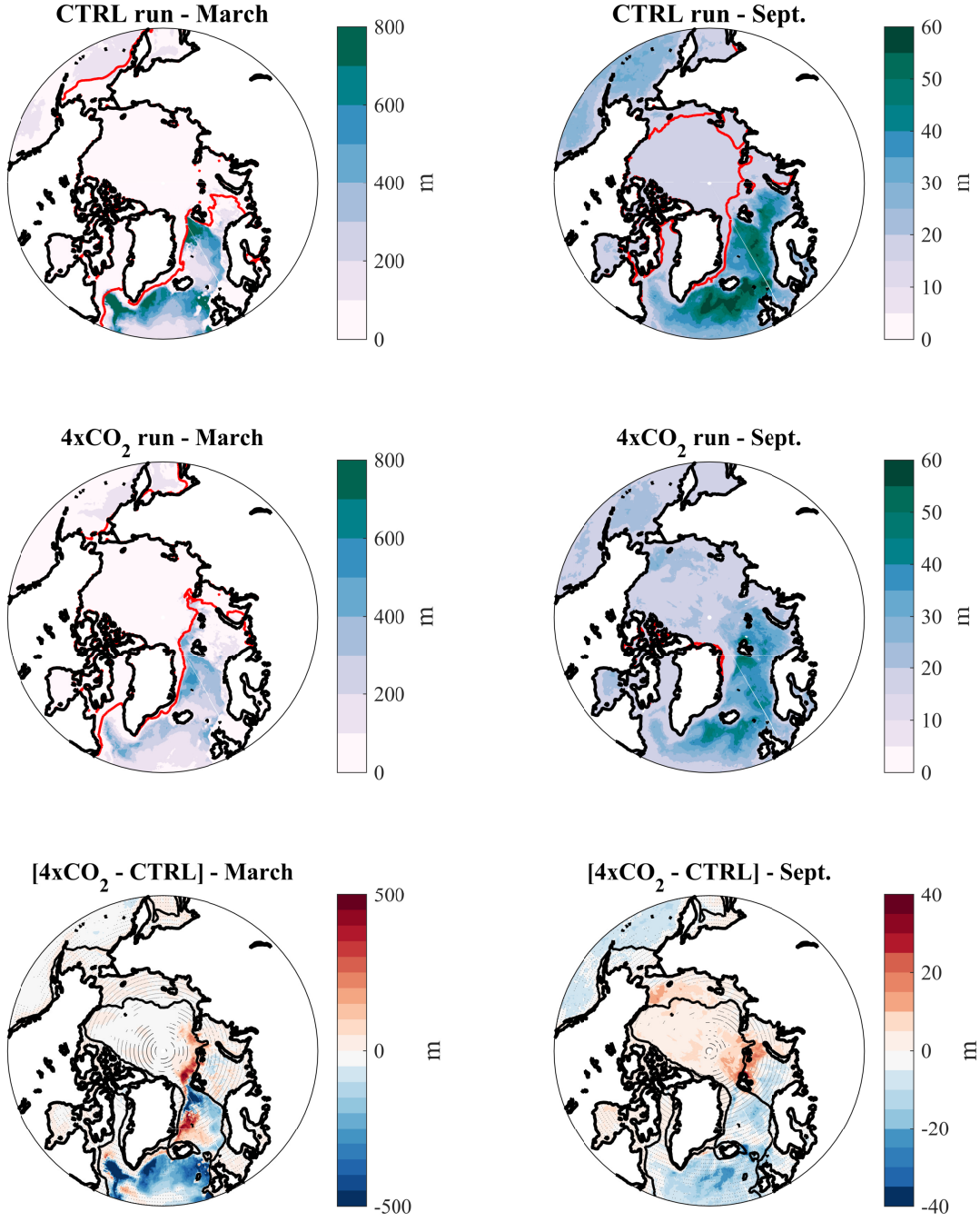


Fig. 1: Mean March and September mixed layer depth (in m) for the *CTRL* and the  $4 \times CO_2$  runs and the difference between the two runs. For the bottom row, black hatching indicates areas where the difference between the two runs is not significant. The red contour corresponds to the location of the sea ice edge (defined as the 15% concentration contour), and the black contour on the bottom panels shows the 500m isobath.

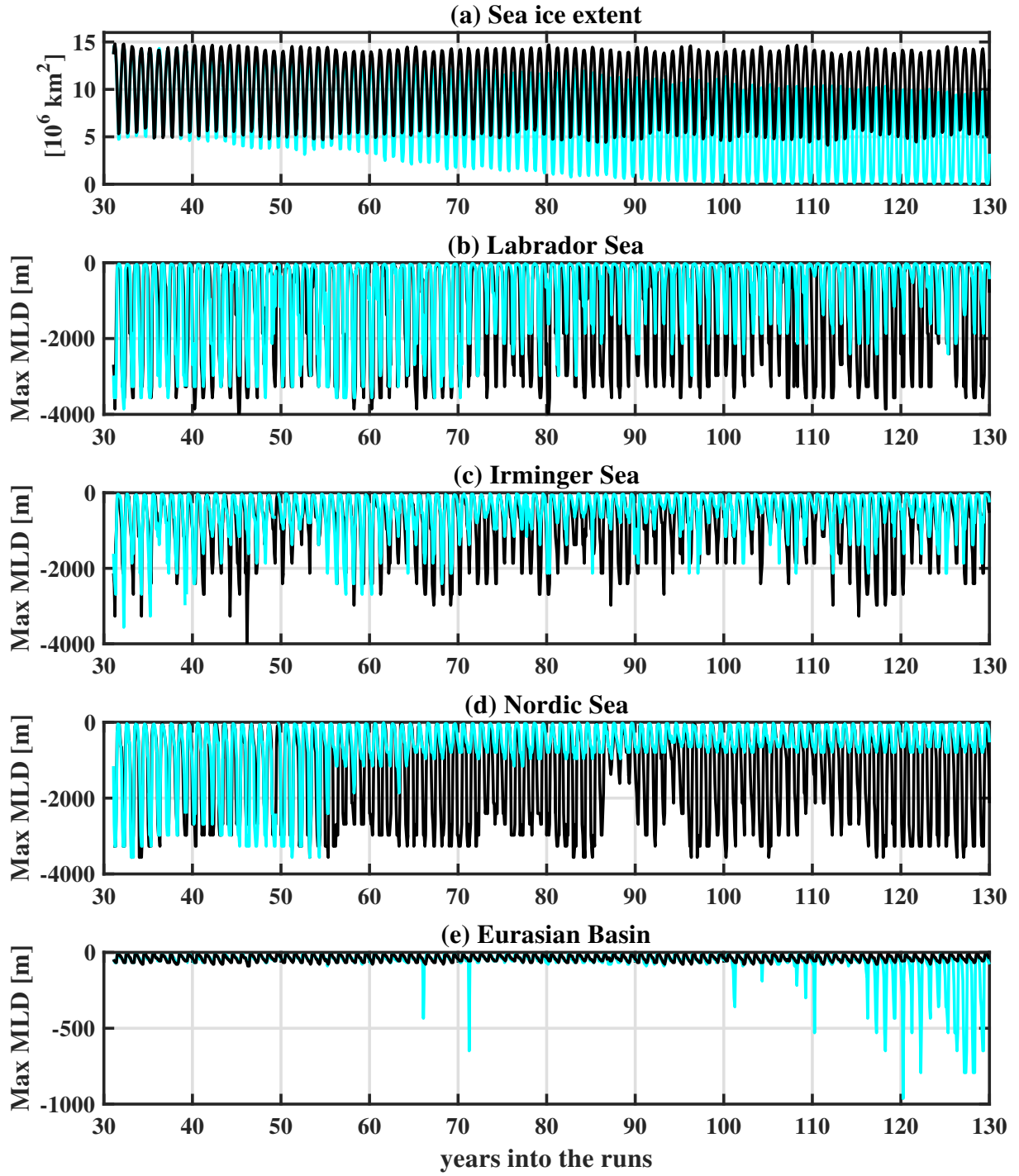


Fig. 2: Time series of (a) sea ice extent, and the maximum MLD detected in (b) the Labrador Sea, (c) the Irminger Sea, (d) the Nordic Sea, and (e) the Eurasian Basin for the last 100 years of the *CTRL* (black) and the  $4 \times CO_2$  (light blue) runs.



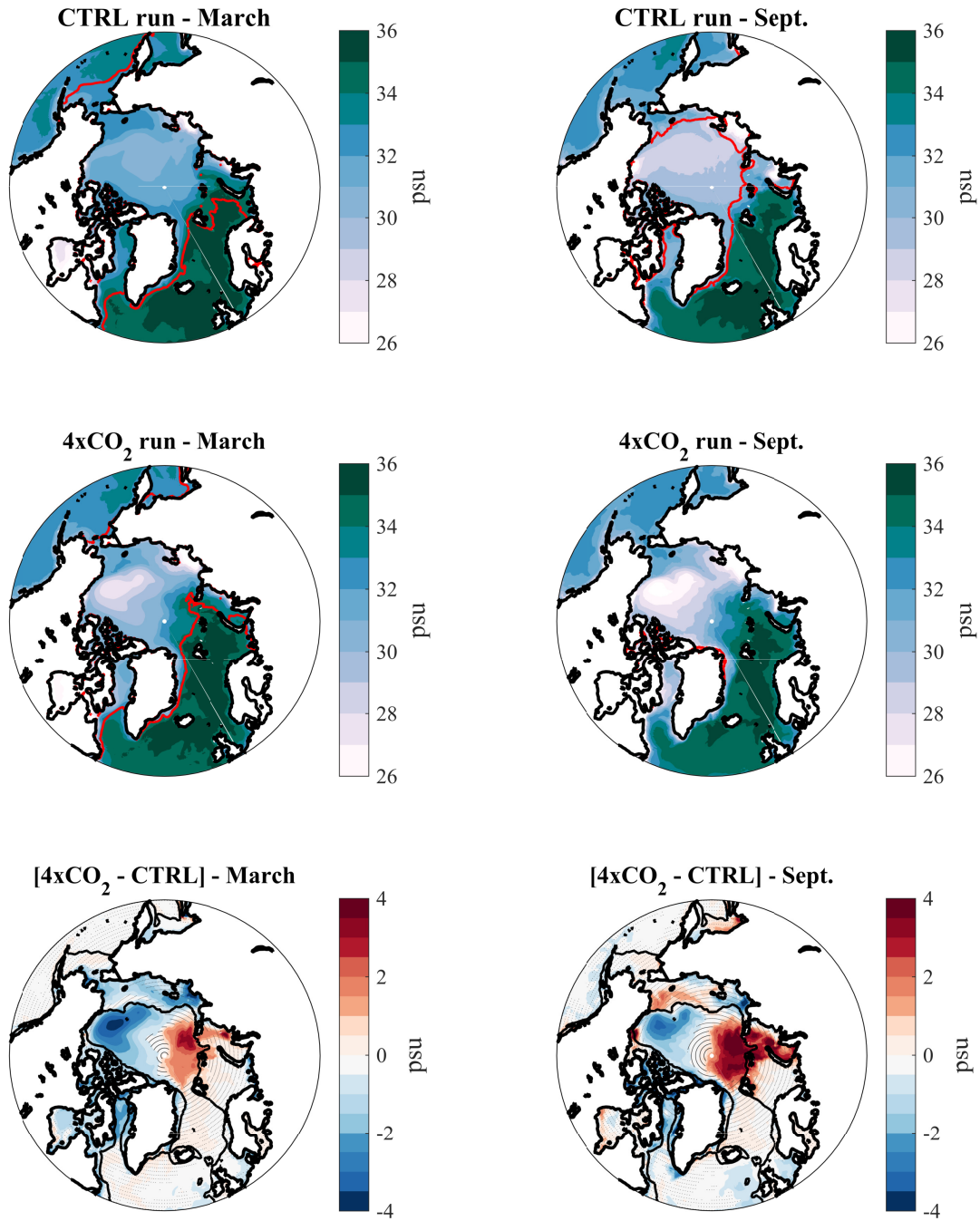


Fig. 3: Mean March and September Sea Surface Temperature (SST, in °C) for the *CTRL* and the  $4 \times CO_2$  runs and the difference between the two runs. For the bottom row, black hatching indicates areas where the difference between the two runs is not significant. The red contour corresponds to the location of the sea ice edge (defined as the 15% concentration contour), and the black contour on the bottom panels shows the 500m isobath.

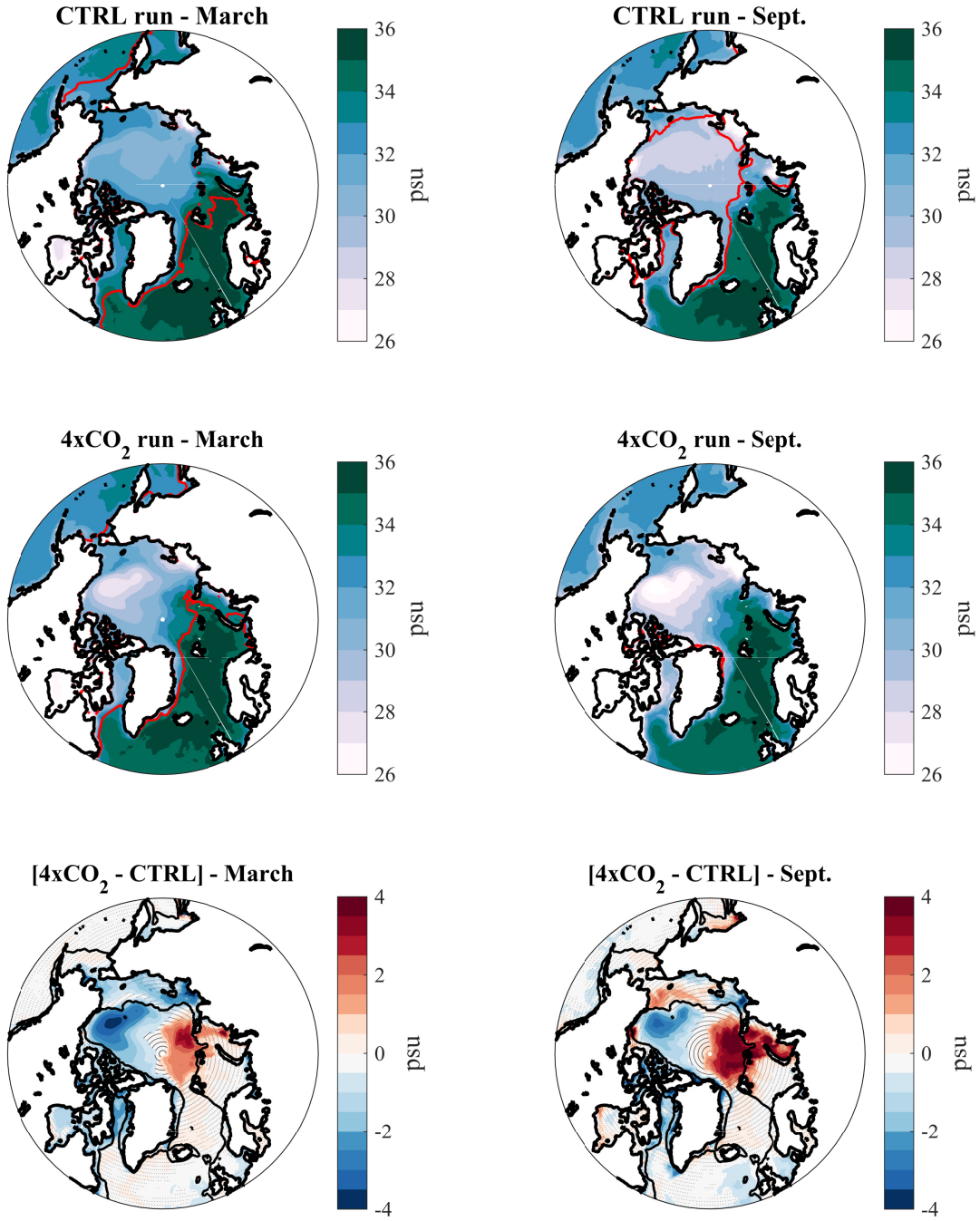


Fig. 4: Mean March and September Sea Surface Salinity (SSS, in psu) for the *CTRL* and the  $4 \times CO_2$  runs and the difference between the two runs. For the bottom row, black hatching indicates areas where the difference between the two runs is not significant. The red contour corresponds to the location of the sea ice edge (defined as the 15% concentration contour), and the black contour on the bottom panels shows the 500m isobath.

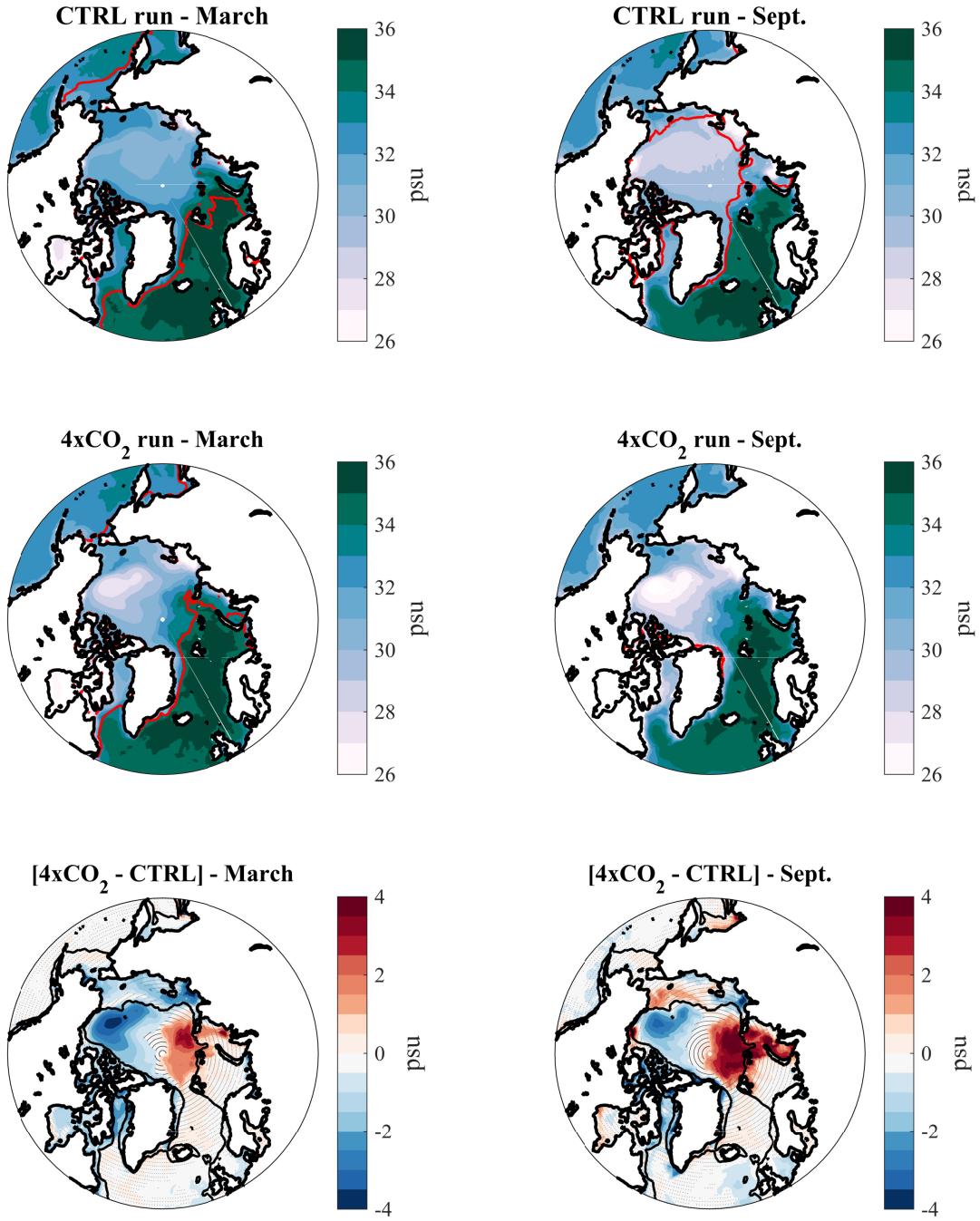


Fig. 5: Mean March and September sea surface potential density ( $\sigma$ , in  $kg/m^3$ ) for the *CTRL* and the  $4 \times CO_2$  runs and the difference between the two runs. For the bottom row, black hatching indicates areas where the difference between the two runs is not significant. The red contour corresponds to the location of the sea ice edge (defined as the 15% concentration contour), and the black contour on the bottom panels shows the 500m isobath.

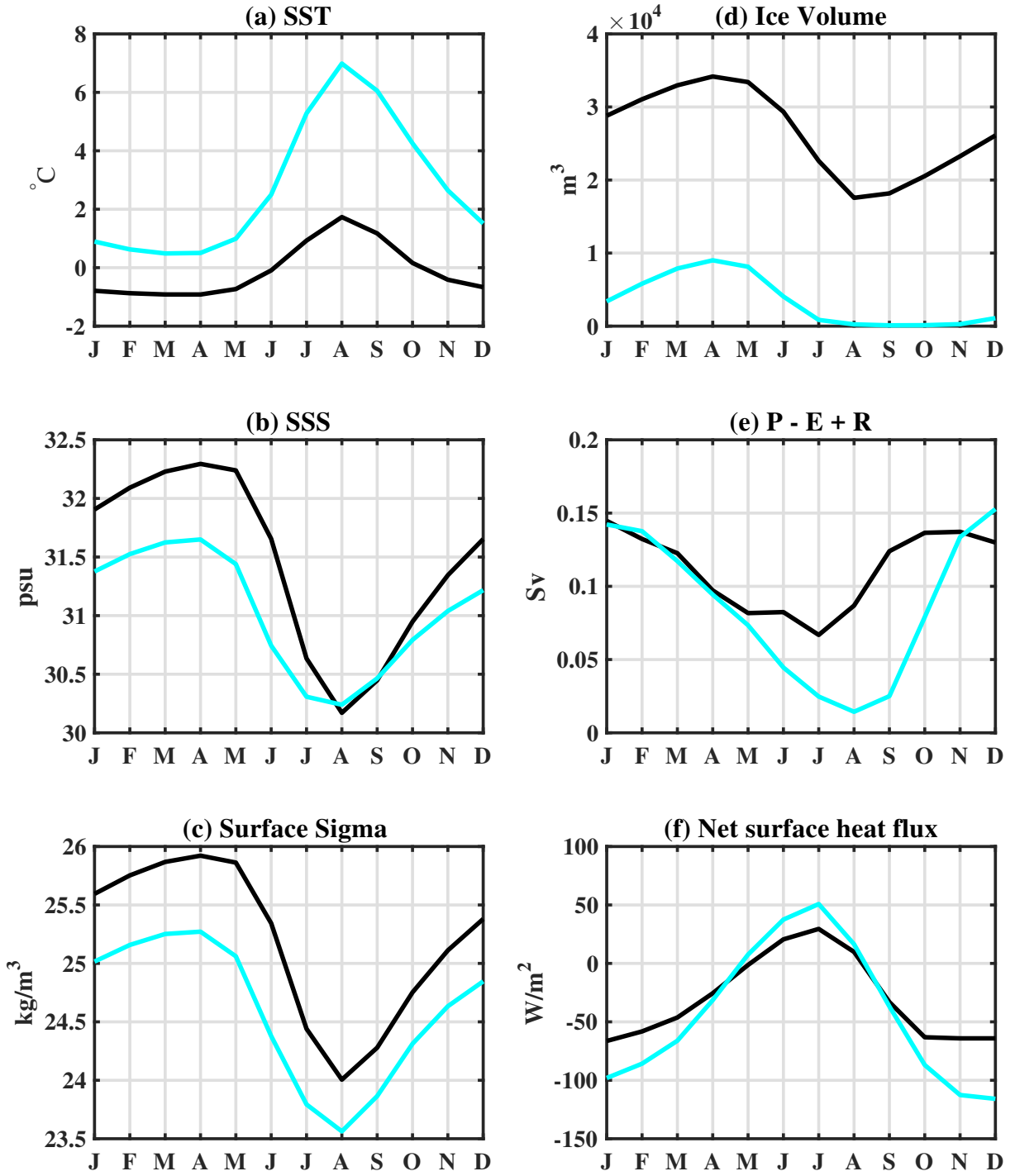


Fig. 6: Mean seasonal cycles of the SST (in  $^\circ C$ ), SSS (in psu), surface density (in  $kg/m^3$ ), ice volume (in  $km^3$ ), sum of precipitation (as water and snow) minus evaporation plus river runoff (in Sv) and net surface heat flux (in  $W/m^2$ ), averaged over the region north of  $65^\circ N$  for the last ten years of the *CTRL* (black) and the  $4 \times CO_2$  (light blue) runs.

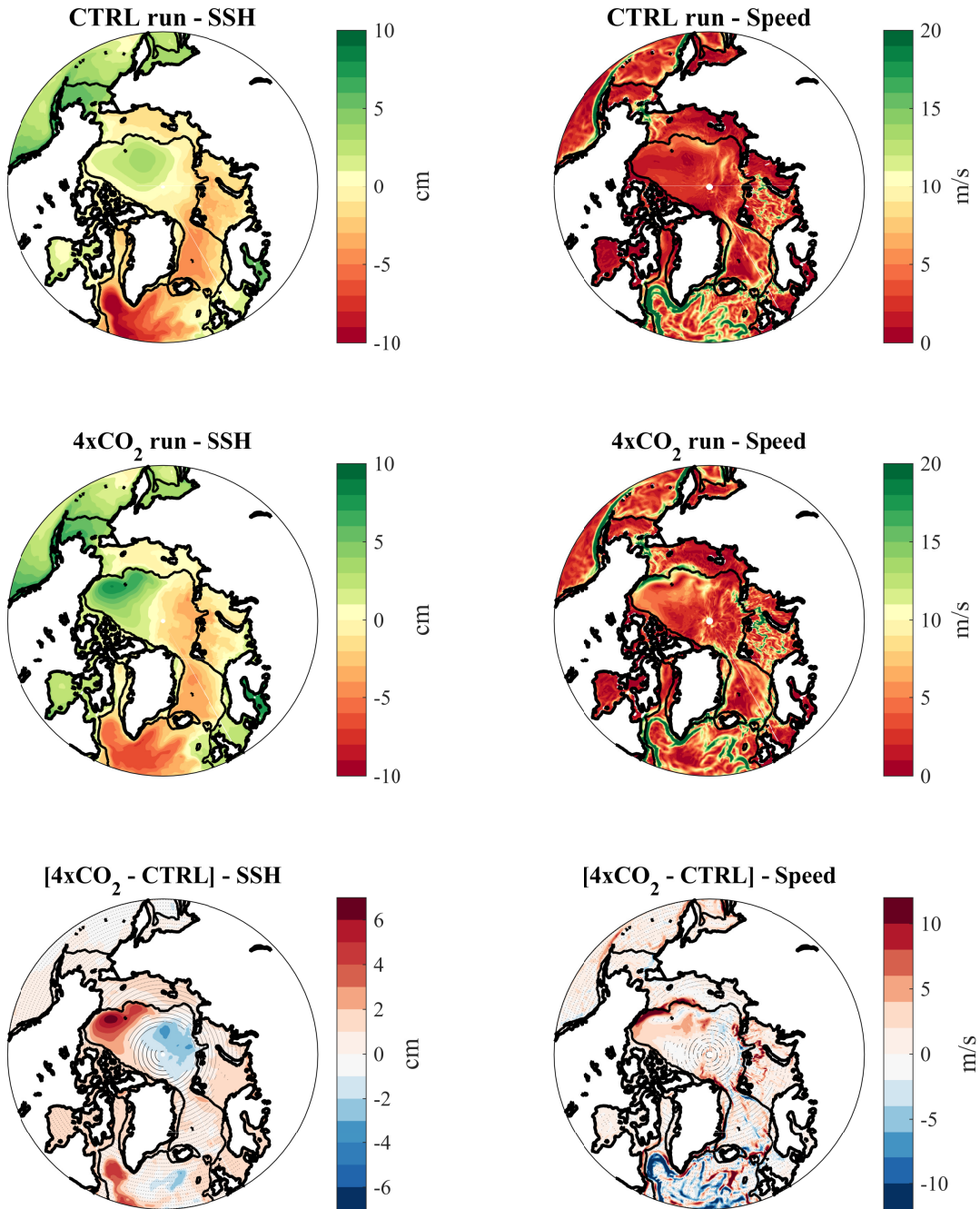


Fig. 7: 10-year averages of Sea Surface Height (SSH in *cm*, left column) and the mean speed over the first 100m (in *cm/s*, right column) for the *CTRL* and the  $4 \times CO_2$  runs and the difference between the two runs. For the bottom row, black hatching indicates areas where the difference between the two runs is not significant. The black contour shows the 500m isobath.



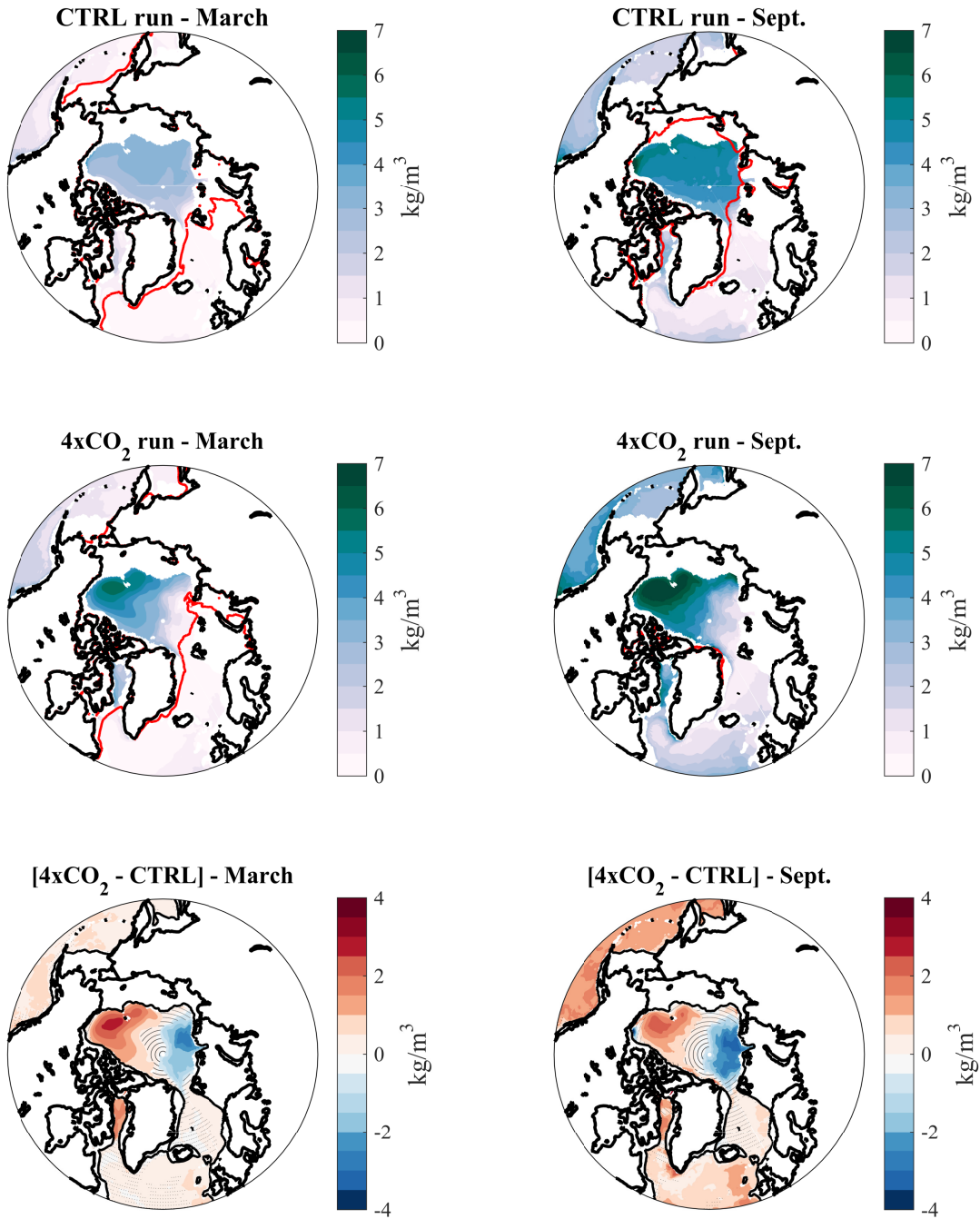


Fig. 8: Mean March and September stratification (defined as the density difference between 500m and the surface, in  $\text{kg/m}^3$ ) for the *CTRL* and the  $4 \times \text{CO}_2$  runs and the difference between the two runs. For the bottom row, black hatching indicates areas where the difference between the two runs is not significant. The red contour corresponds to the location of the sea ice edge (defined as the 15% concentration contour), and the black contour on the bottom panels shows the 500m isobath.

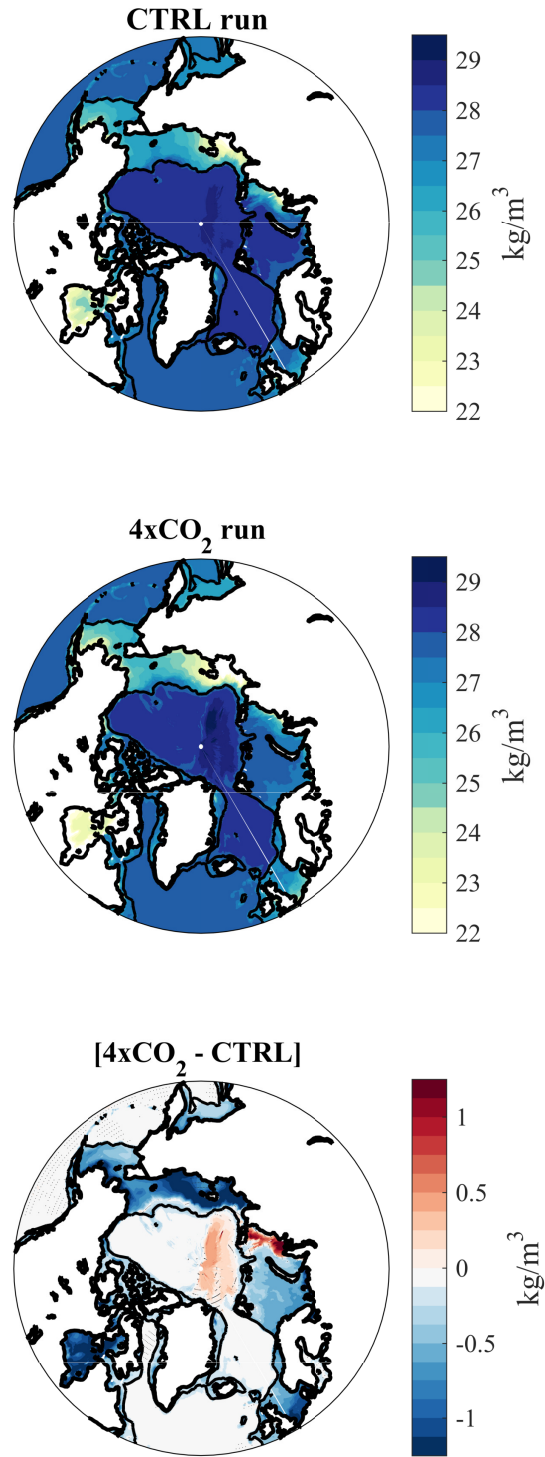


Fig. 9: 10-year average of the bottom density (in  $\text{kg/m}^3$ ) for the *CTRL* and the  $4 \times \text{CO}_2$  runs and the difference between the two runs. For the bottom row, black hatching indicates areas where the difference between the two runs is not significant. Bottom density corresponds to the density of the last ocean model vertical level at each grid point, and is computed relative to the surface. The black contour shows the 500m isobath.

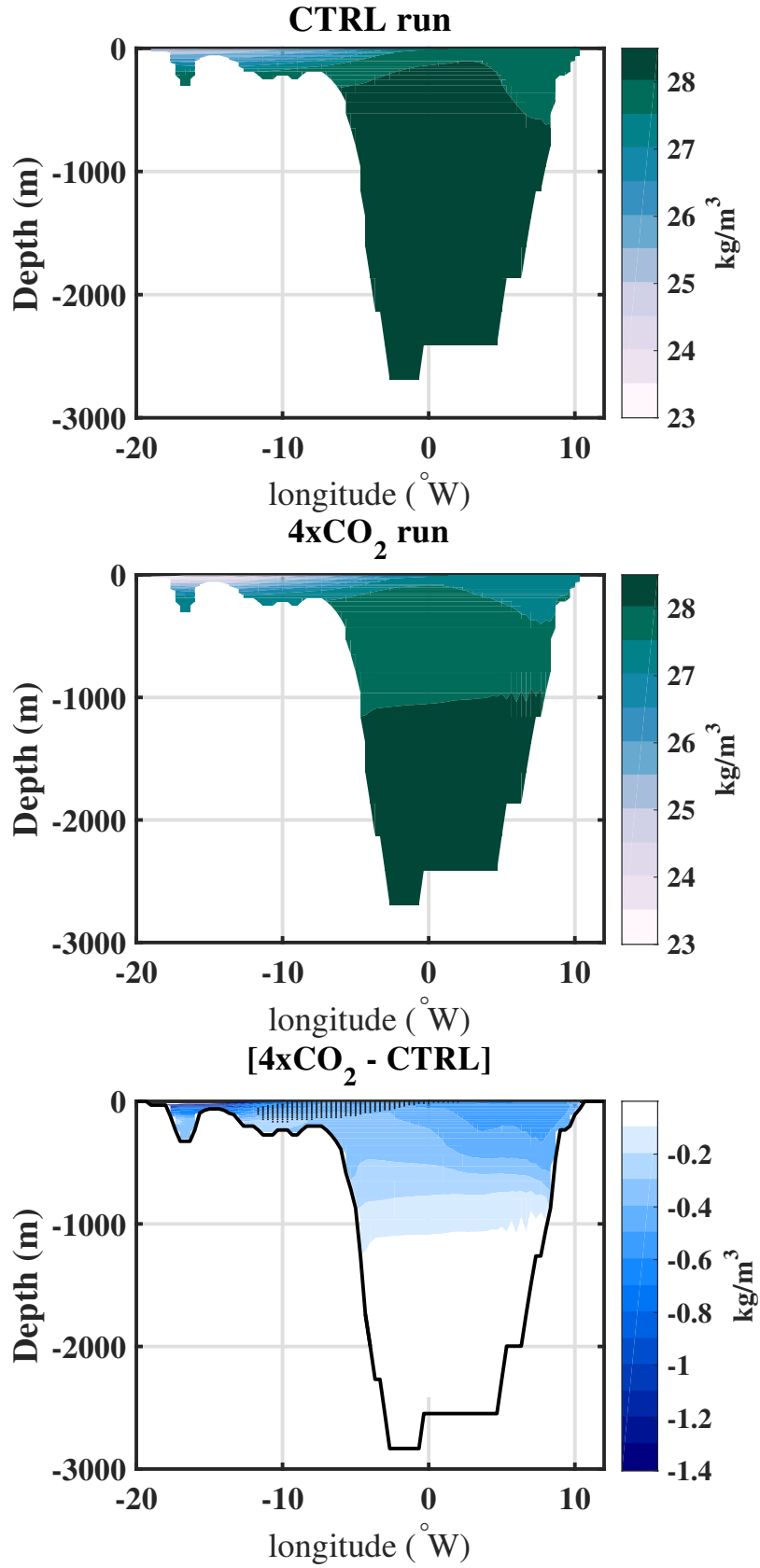


Fig. 10: Section across Fram Strait of the 10-year average density (in  $kg/m^3$ ) for the *CTRL* and the  $4 \times CO_2$  runs and the difference between the two runs. For the bottom row, black hatching indicates the parts of the strait where the difference between the two runs is not significant.